

## Morphology-tuned Synthesis of MgCo<sub>2</sub>O<sub>4</sub> Arrays on Graphene Coated Nickel Foam for High-Rate Supercapacitor Electrode

Xiangfeng Guan<sup>1,2</sup>, Qiurong Wang<sup>1</sup>, Peihui Luo<sup>2</sup>, Yunlong Yu<sup>2</sup>, Xiaoyan Li<sup>1</sup>, Yu Zhang<sup>2</sup>, Dagui Chen<sup>2,\*</sup>

<sup>1</sup> College of Electronics and Information Science, Fujian Jiangxia University, Fuzhou, Fujian 350108, P. R. China

<sup>2</sup> Organic Optoelectronics Engineering Research Center of Fujian's Universities, Fuzhou, Fujian 350108, P. R. China

\*E-mail: [dgchen@fjixu.edu.cn](mailto:dgchen@fjixu.edu.cn)

Received: 4 November 2017 / Accepted: 24 December 2017 / Published: 5 February 2018

Rational design of advanced electrode materials is highly desirable and technically important for developing high-performance electrochemical supercapacitors. In this work, we have successfully synthesized MgCo<sub>2</sub>O<sub>4</sub> nanosheet, nanobelt, and nanowire arrays on graphene-coated nickel foam by a facile three-step synthesis method. The morphologies of MgCo<sub>2</sub>O<sub>4</sub> arrays can be readily tuned by changing the volume ratio of DEG and deionized water. Moreover, when explored as supercapacitor electrode, the MgCo<sub>2</sub>O<sub>4</sub> nanowire arrays electrode exhibits superior high-rate electrochemical performance, which delivers an optimal specific capacitance of 500 F g<sup>-1</sup> at a high current density of 50 A g<sup>-1</sup> and exhibits good cycling performance. This work provides alternative strategies for constructing advanced supercapacitor electrode with superior high-rate performance.

**Keywords:** Morphology control; MgCo<sub>2</sub>O<sub>4</sub> arrays; Graphene; Supercapacitors

### 1. INTRODUCTION

Supercapacitors (SCs) have been much concerned due to their relatively high power density, robust cycle life, and excellent rate capability [1-3]. According to the energy storage mechanisms, there are two types of SCs: electric double layer capacitors and pseudocapacitors. The former involves physical charge accumulation and the latter is related with Faradaic redox reaction [4, 5]. Electrode materials are the key component for SCs, which ultimately determine their electrochemical performance. Up to now, various materials including conductive polymers [6-8], carbonaceous material [9-11], and metal oxides [12-15] have been intensively investigated for SCs electrodes. In particular, transition metal oxides have attracted extensive attention due to the excellent redox charge transfer originated from their multiple oxidation states [16].

Ternary Mg-Co oxide,  $\text{MgCo}_2\text{O}_4$ , is an important multifunctional material, which has been widely applied in catalysts and lithium-ion batteries because of their interesting catalytic and electrochemical properties [17, 18]. Recently,  $\text{MgCo}_2\text{O}_4$  has been successfully used as electrode material for pseudocapacitors due to the synergistic effects from cobalt and magnesium [19-24]. For instances,  $\text{MgCo}_2\text{O}_4$  nanorods synthesized via a co-precipitation method showed a high specific capacitance of  $752 \text{ F g}^{-1}$  at  $2 \text{ mA cm}^{-1}$  [19].  $\text{MgCo}_2\text{O}_4$  nanoparticles synthesized through a molten salt method displayed a specific capacitance of  $321 \text{ F g}^{-1}$  at  $0.5 \text{ A g}^{-1}$  and showed a stable cycling performance [20].  $\text{MgCo}_2\text{O}_4/\text{rGO}$  composites synthesized through a hydrothermal approach demonstrated a specific capacitance of  $570 \text{ F g}^{-1}$  at  $1 \text{ A g}^{-1}$  and the capacity retained 95% of its initial value after 5000 cycles [21]. Three dimensional  $\text{MgCo}_2\text{O}_4$  nanocone/nickel foam fabricated by a hydrothermal synthesis route delivered a high specific capacitance of  $750 \text{ F g}^{-1}$  at  $1 \text{ A g}^{-1}$  and relatively low specific capacitance of  $445.7 \text{ F g}^{-1}$  at  $20 \text{ A g}^{-1}$  [22]. Although great progress has been made, in comparison with its theoretical capacitance (about  $3122 \text{ F g}^{-1}$ ), the practical specific capacitance of  $\text{MgCo}_2\text{O}_4$  is not satisfying and the rate capability under high charge-discharge current density needs further improved.

In this work,  $\text{MgCo}_2\text{O}_4$  arrays on graphene coated nickel foam were fabricated via chemical vapor deposition, hydrothermal, and heat-treatment methods. Without any templates and additives, the morphologies of  $\text{MgCo}_2\text{O}_4$  arrays can be easily tuned to nanowires, nanobelts, and nanosheets by adjusting the reaction solvent components. When evaluated as electrodes material for supercapacitor, the as-synthesized  $\text{MgCo}_2\text{O}_4$  nanowire arrays/G-NF exhibits superior electrochemical performance, which is featured by high specific capacitance, excellent rate capability, and good cycling performance.

## 2. EXPERIMENTAL

### 2.1 Materials

Analytical grade chemicals of magnesium acetate ( $\text{C}_4\text{H}_6\text{MgO}\cdot 4\text{H}_2\text{O}$ ), cobaltous acetate ( $\text{C}_4\text{H}_6\text{CoO}_4\cdot 4\text{H}_2\text{O}$ ), urea ( $\text{CO}(\text{NH}_2)_2$ ), diethylene glycol (DEG) were used as the starting materials without further purification.

### 2.2 Synthesis of graphene coated nickel foam hybrid structure (G-NF)

Chemical vapor deposition (CVD) method was used to synthesize graphene coated nickel foam according to the previous report with a slight modification [25]. Firstly, one piece of nickel foam was cleaned and put into a quartz tube, which was heated at  $1000 \text{ }^\circ\text{C}$  for 60 min with a heating rate of  $30 \text{ }^\circ\text{C}/\text{min}$  in the flowing mixed gas of  $\text{H}_2$  (10 sccm) and Ar (300 sccm). Secondly,  $\text{CH}_4$  (60sccm) was loaded into the quartz tube for another 15 min. Finally, the furnace was fast cooled down under a  $\text{H}_2/\text{Ar}$  flow and then the multilayer graphene film/ nickel foam (G-NF) hybrid structure were obtained.

### 2.3 Synthesis of MgCo<sub>2</sub>O<sub>4</sub> arrays on G-NF

A typical synthesis process of MgCo<sub>2</sub>O<sub>4</sub> nanowire arrays was conducted as follows: 0.4204 g CO(NH<sub>2</sub>)<sub>2</sub>, 0.2145 g C<sub>4</sub>H<sub>6</sub>MgO•4H<sub>2</sub>O, and 0.4982 g C<sub>4</sub>H<sub>6</sub>CoO<sub>4</sub>•4H<sub>2</sub>O were dissolved in a mixed reaction solvent composed of 10 mL deionized water and 30 mL diethylene glycol (DEG). Then a piece of as-prepared G-NF (1 × 4 × 0.1 cm) was totally immersed into the above solvent and placed into a Teflon-lined stainless steel autoclave to react at 180 °C for 4 h. The solvothermally treated G-NF was rinsed with deionized water and dried several times. Finally, the samples were annealed in Ar flow at 400 °C for 2 h to obtain MgCo<sub>2</sub>O<sub>4</sub> nanowire arrays on G-NF. The MgCo<sub>2</sub>O<sub>4</sub> nanobelt and nanosheet on G-NF were synthesized with a similar process, except that the components of the reaction solvent were changed. For MgCo<sub>2</sub>O<sub>4</sub> nanobelt, the reaction solvent was composed of 20 mL deionized water and 20 mL DEG; for MgCo<sub>2</sub>O<sub>4</sub> nanosheet, only deionized water was used as reaction solvent.

### 2.4 Materials characterization

The samples were intensively characterized via X-ray diffraction (XRD), Raman spectrum, field emission scanning electron microscopy (FE-SEM), energy-dispersive X-ray spectroscopy (EDS), transmission electron microscopy (TEM), and X-ray photoelectron spectroscopy (XPS).

### 2.5 Electrochemical characterization

The electrochemical performances were performed on an electrochemical workstation (CHI 660E) and tested in a three-electrode system. The 6.0 M KOH aqueous solution, Ag-AgCl, and Pt electrode were used as the electrolyte, reference, and counter electrode, respectively. The as-prepared MgCo<sub>2</sub>O<sub>4</sub> arrays/G-NF samples were used as the working electrodes. Cyclic voltammetry (CV) measurement was performed at increasing scan rates from 5 to 100 mV s<sup>-1</sup>. The galvanostatic charge-discharge (GCD) was conducted at varied current densities ranging from 1 to 50 A g<sup>-1</sup>. Electrochemical impedance spectroscopy (EIS) was carried out in the frequency range from 0.01 Hz to 100 kHz with a potential amplitude of 5 mV. The specific capacitance (C<sub>s</sub>) is calculated according to the following equation:

$$C_s = \frac{I\Delta t}{m\Delta V} \quad (1)$$

Where  $I$ ,  $\Delta t$ ,  $m$ ,  $\Delta V$  represents the discharge current, time, the mass of active materials, and the potential drop, respectively.

## 3. RESULTS AND DISCUSSION

### 3.1 Morphology and structural analysis

Figure 1 shows the schematic diagram illustrating the synthesis processes of MgCo<sub>2</sub>O<sub>4</sub> arrays on G-NF. Firstly, G-NF was fabricated by growing graphene on nickel foam by CVD method.

Secondly, the  $\text{MgCo}_2\text{O}_4$  precursor arrays were homogeneously grown on the surface of G-NF by solvothermal synthesis. Finally,  $\text{MgCo}_2\text{O}_4$  nanostructure arrays/G-NF were obtained by annealing the  $\text{MgCo}_2\text{O}_4$  precursor in Ar. By simply adjusting the solvent ratio of DEG/ $\text{H}_2\text{O}$ , the morphologies of  $\text{MgCo}_2\text{O}_4$  arrays can be effectively tuned. Briefly, with the increase of DEG content, the morphology of  $\text{MgCo}_2\text{O}_4$  arrays transformed from 2D nanosheet to 1D nanobelt and nanowire.

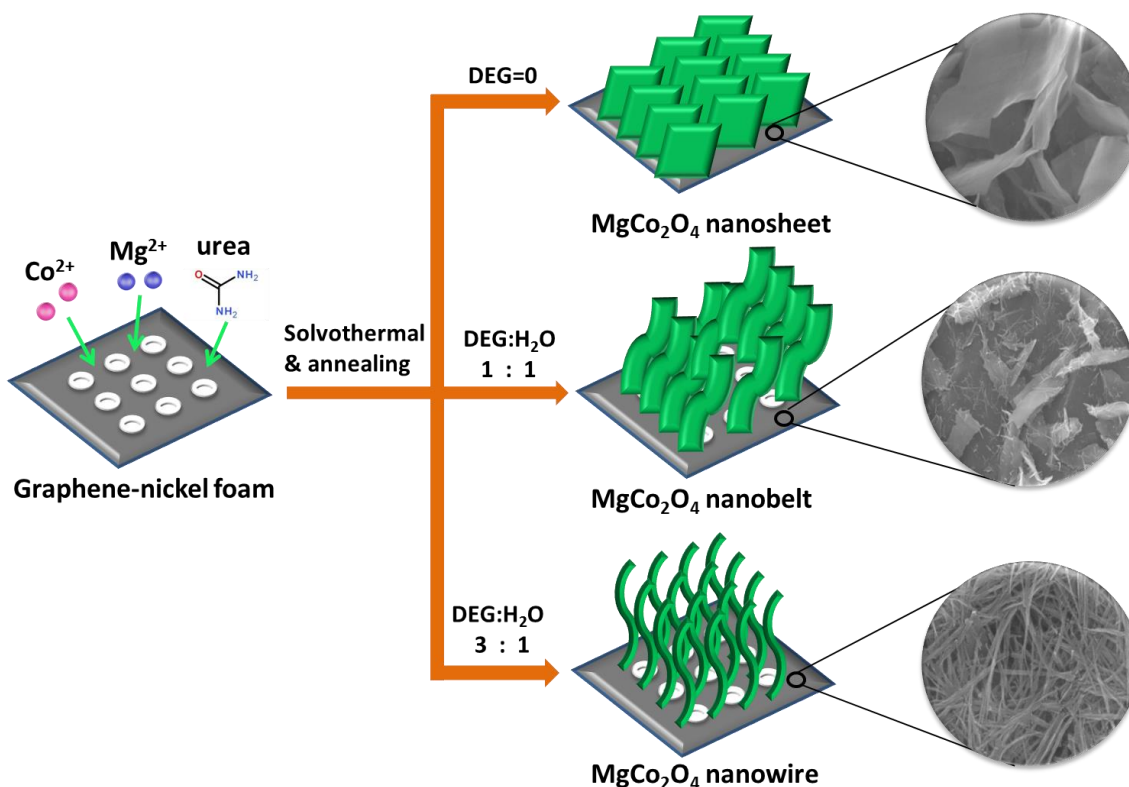
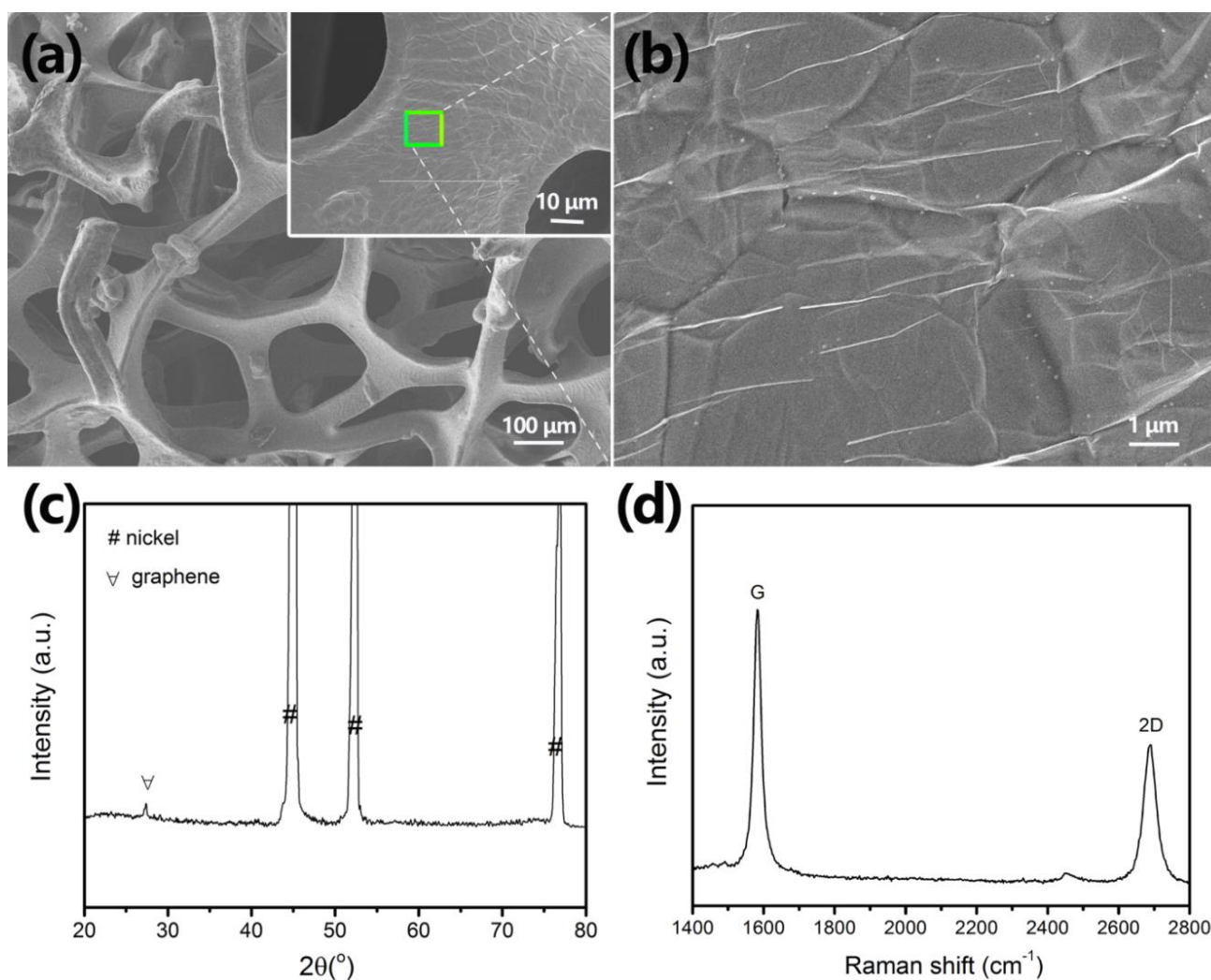


**Figure 1.** Schematic diagram for the three-step synthesis processes of  $\text{MgCo}_2\text{O}_4$  nanosheet, nanobelt, and nanowire arrays on G-NF: The first step is the formation of G-NF by the CVD method; the second step is the solvothermal synthesis of  $\text{MgCo}_2\text{O}_4$  precursor array on the surface of G-NF; the third step is the formation of  $\text{MgCo}_2\text{O}_4$  nanosheet, nanobelt, and nanowire arrays/G-NF by annealing the  $\text{MgCo}_2\text{O}_4$  precursor in Ar.

The morphology and structure information of the G-NF was shown in Figure 2. It can be seen that the G-NF presents three-dimensional cross-linked and porous structure (Figure 2a) which was completely coated with a continuous thin film (Figure 2b). Figure 2c shows the XRD results of the G-NF. The three intense diffraction peaks between  $40$  and  $80^\circ$  can be well indexed to the planes of (111), (200) and (220) of the nickel foam (No. 87-0712, JCPDS card). The weak diffraction peak around  $26^\circ$  is attributed to the (002) plane of graphene [26]. Therefore, the nickel foam was completely covered by a thin layer of graphene. It is also supported by Raman spectrum of the G-NF, which shows two distinctive peaks corresponding to the G band ( $1585\text{ cm}^{-1}$ ) and 2D band ( $2689\text{ cm}^{-1}$ ) of graphene (Figure 2d).

Figure 3 shows the SEM images of the  $\text{MgCo}_2\text{O}_4$  arrays/G-NF samples. As stated above, when we only changed the volume ratio of DEG/ deionized water and kept other reaction conditions

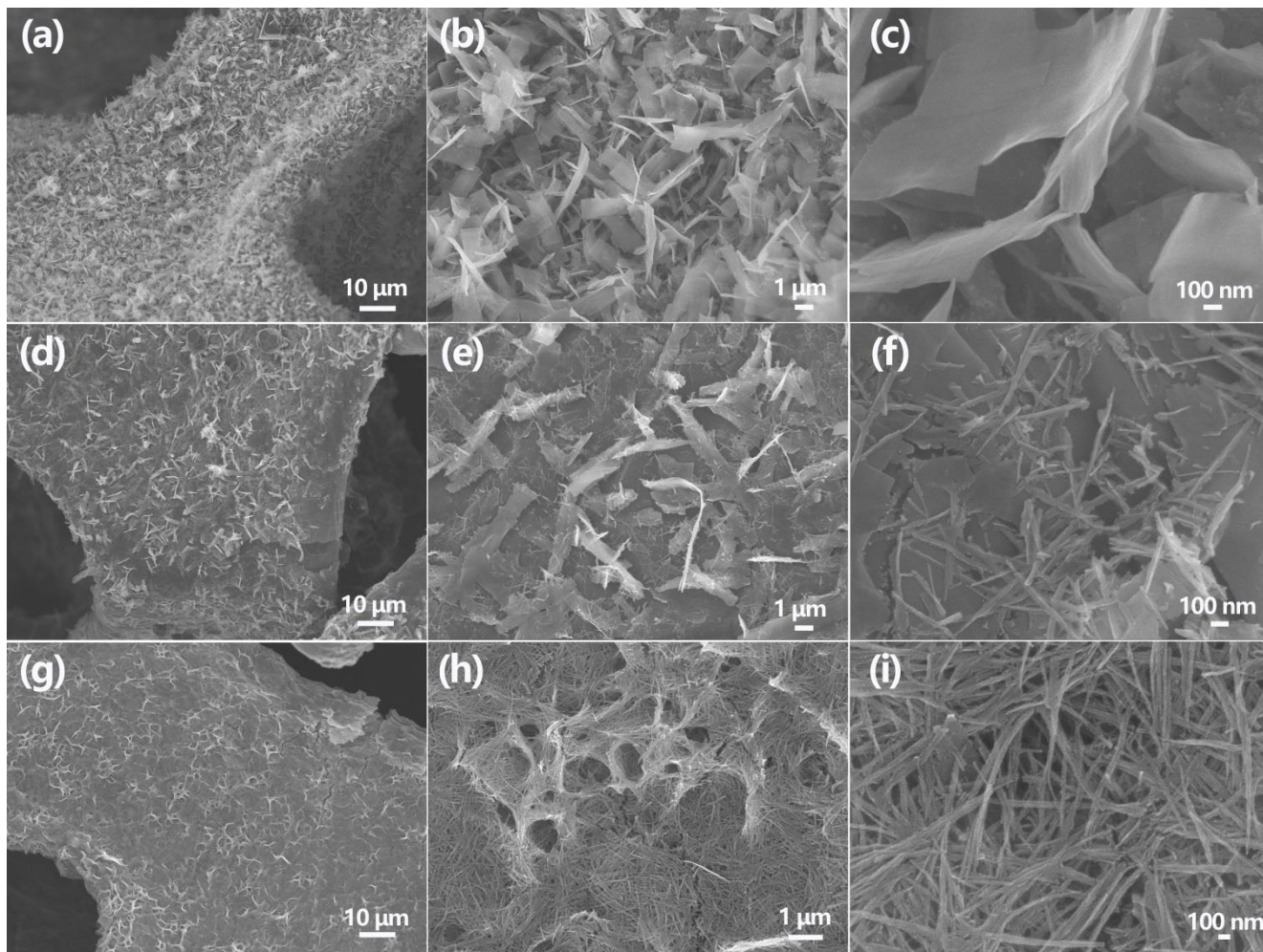
unchanged,  $\text{MgCo}_2\text{O}_4$  arrays with distinct morphologies can be prepared (as shown in Figure 1). It is seen that all  $\text{MgCo}_2\text{O}_4$  arrays are homogeneously grown on the G-NF (Figure 3a, 3d, and 3g). When no DEG was used,  $\text{MgCo}_2\text{O}_4$  nanosheets with about 3  $\mu\text{m}$  in width and 50 nm in thickness were obtained (Figure 3b and c). When the volume ratio of DEG/water is 1:1,  $\text{MgCo}_2\text{O}_4$  nanobelts with about 2  $\mu\text{m}$  in width and 10  $\mu\text{m}$  in length were formed (Figure 3e and f), as well as small amount of nanorods. When the volume ratio of DEG/water increases to 3:1,  $\text{MgCo}_2\text{O}_4$  nanowires with about 50 nm in width and 2  $\mu\text{m}$  in length was achieved (Figure 3h and i). Apparently, the morphologies of  $\text{MgCo}_2\text{O}_4$  arrays can be readily tuned by changing the volume ratio of DEG and deionized water.



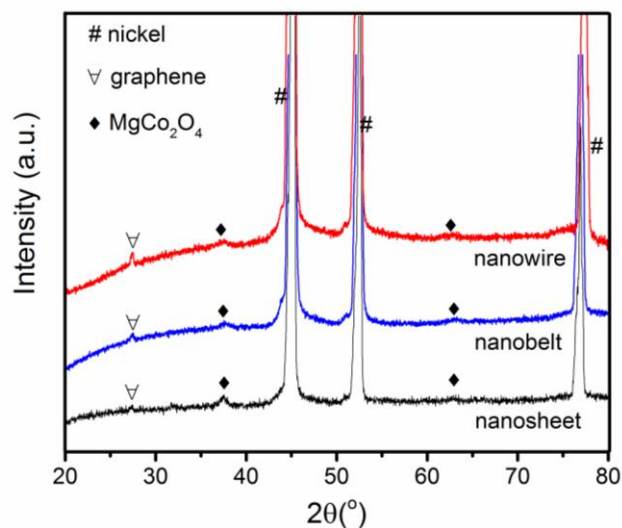
**Figure 2.** (a) Low magnification SEM images, (b) high magnification SEM images of the marked rectangular area in the inset of (a), (c) XRD pattern, and (d) Raman spectra of graphene-coated nickel foam.

Figure 4 shows the XRD patterns of as-prepared  $\text{MgCo}_2\text{O}_4$  arrays on G-NF with different morphologies. Except for the three strong diffraction peaks attributed to metal nickel (marked as #), the diffraction peaks (marked as  $\blacklozenge$ ) indexed to (311) and (400) planes of  $\text{MgCo}_2\text{O}_4$  phase (No. 81-

0667, JCPDS card) can be seen. Specially, the diffraction peak of graphene is still obviously observed, indicating that  $MgCo_2O_4$  phase was successfully formed on graphene-coated nickel foam.



**Figure 3.** Low-magnification and high-magnification SEM images of the  $MgCo_2O_4$  arrays with different morphologies: (a-c) nanosheets, (d-f) nanobelts, and (g-i) nanowires.



**Figure 4.** XRD patterns of as-prepared  $MgCo_2O_4$  arrays on G-NF with different morphologies.

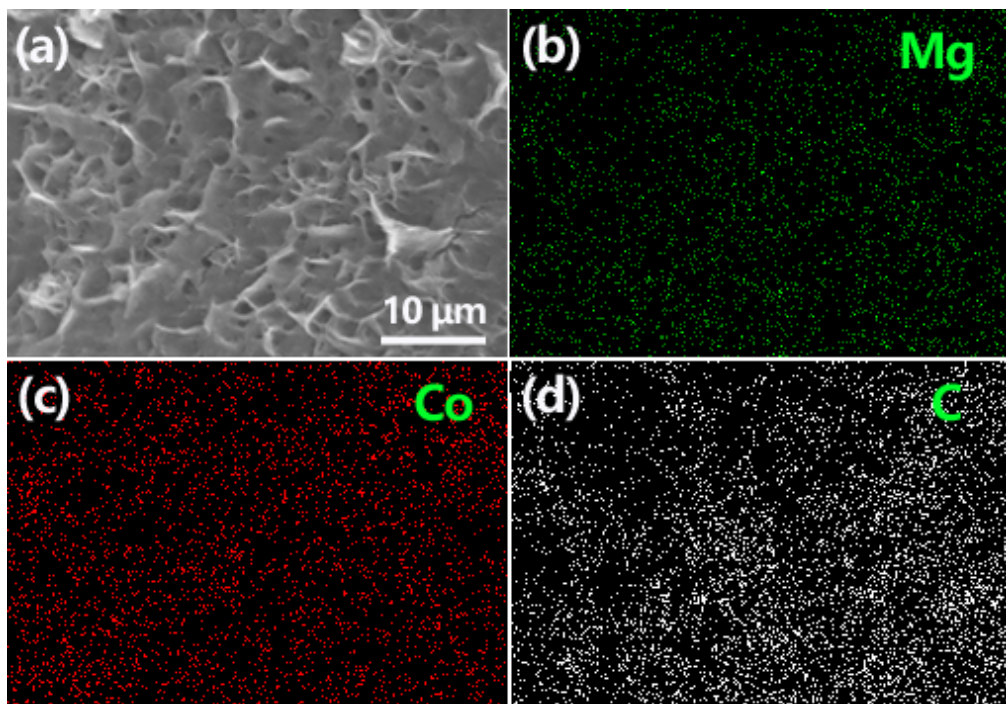


**Figure 5.** (a) SEM image and (b-d) EDS elemental mapping of the  $\text{MgCo}_2\text{O}_4$  nanowire arrays/G-NF: (b) Mg, (c) Co, and (d) C.

To investigate the component distribution of the  $\text{MgCo}_2\text{O}_4$  nanowire/G-NF sample, EDS elemental mapping was performed. Figure 5a shows the low magnification SEM image of the  $\text{MgCo}_2\text{O}_4$  nanowires arrays on G-NF. As shown in Figure 5b and c, elemental mapping images revealed the uniform distribution of Mg and Co in the  $\text{MgCo}_2\text{O}_4$  nanowire/G-NF sample, implying the formation of pure  $\text{MgCo}_2\text{O}_4$  phase instead of oxide composites. Moreover, C element is also homogeneously distributed (Figure 5d), further demonstrating that graphene thin film was well retained.

TEM, high-resolution TEM (HRTEM), and selected-area electron diffraction (SAED) were performed to get further information of the  $\text{MgCo}_2\text{O}_4$  nanowire arrays/G-NF sample. Figure 6a shows the TEM image of  $\text{MgCo}_2\text{O}_4$  nanowires peeled off from G-NF. It is seen that the nanowires are 20-30 nm in width, which are assembled by many nanoparticles stacking together, showing mesoporous characteristic. Figure 6b and c show the corresponding HRTEM images of the marked rectangular area in Figure 6a. It is found that the distinct interlayer spacings of 0.24 and 0.20 nm, which corresponds to the (311) and (400) planes of the  $\text{MgCo}_2\text{O}_4$ . The corresponding SAED patterns (Figure 6d) also indicated the polycrystalline characteristic of  $\text{MgCo}_2\text{O}_4$ .

The elemental compositions and oxidation state of the  $\text{MgCo}_2\text{O}_4$  nanowires/G-NF sample are studied by XPS (Figure 7). The C 1s peak can be deconvoluted into three curves in the range of 287-292 eV. The Mg 2p peak is about 49.6 eV (Figure 4b), which is in accordance with the previous literature reports [27]. The spectrum of Co 2p (Figure 7c) shows several asymmetric peaks, which consist of several overlapping features originating from the 2p<sub>3/2</sub> and 2p<sub>1/2</sub> peaks due to  $\text{Co}^{2+}$  and  $\text{Co}^{3+}$  together with the associated satellite structure.

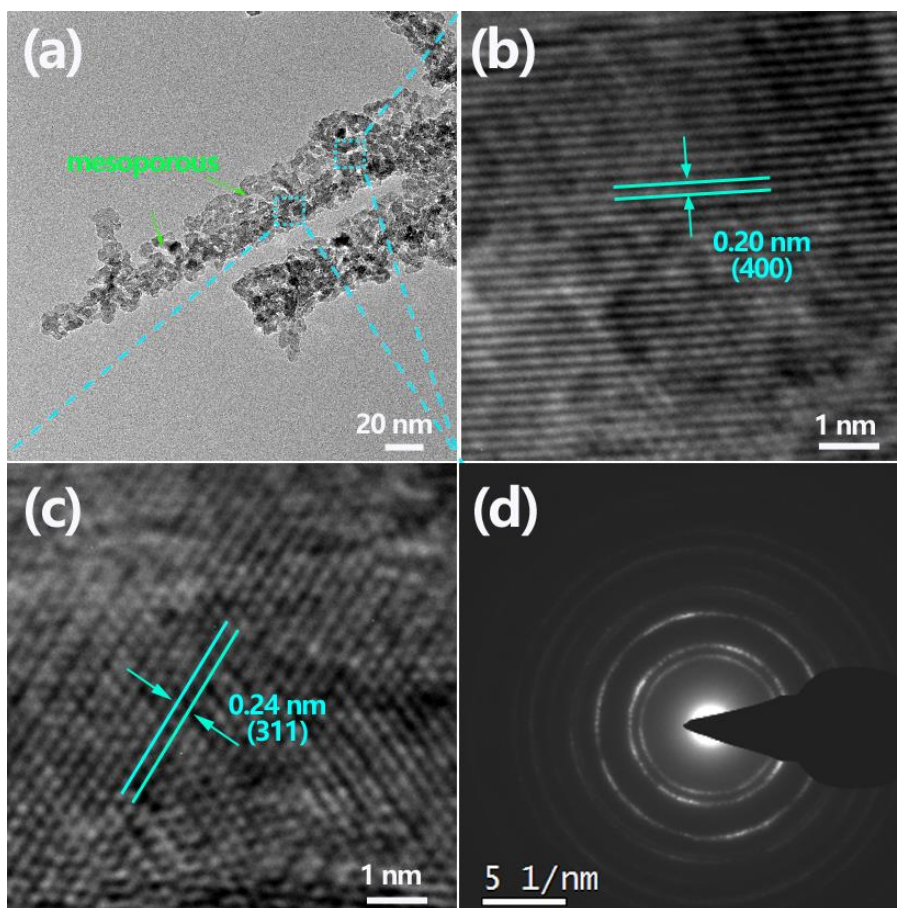


**Figure 6.** (a) TEM image of the  $\text{MgCo}_2\text{O}_4$  nanowire peeled off from G-NF; (b)(c) HRTEM images of the marked rectangular areas in (a), and (d) the SAED pattern of the same  $\text{MgCo}_2\text{O}_4$  nanowires.

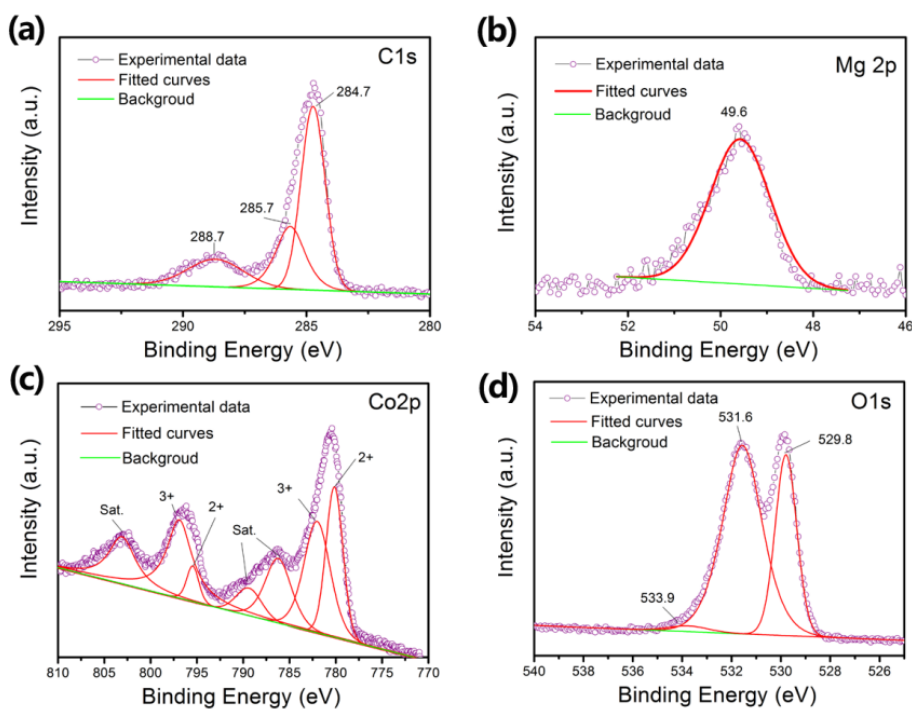


**Figure 7.** Binding energy spectra of the  $\text{MgCo}_2\text{O}_4$  nanowire/G-NF sample: (a) C 1s, (b) Mg 2p, (c) Co 2p, (d) O 1s.

The peaks at 782.1 and 796.9 eV are related with  $\text{Co}^{3+}$  component and the peaks located at 780.2 and 795.5 eV are related with  $\text{Co}^{2+}$  component in  $\text{MgCo}_2\text{O}_4$ . The satellite peak located at 786.3 eV and 789.5 eV is associated with  $\text{Co}^{2+}$  species and  $\text{Co}^{3+}$  component, respectively [28]. The satellite peak located at 803.1 eV is associated with  $\text{Co}^{2+}/\text{Co}^{3+}$  [29, 30]. Therefore, both  $\text{Co}^{2+}$  and  $\text{Co}^{3+}$  existed in as-prepared  $\text{MgCo}_2\text{O}_4$ . The O 1s spectrum (Figure 4d) can be deconvoluted into three peaks at 529.8, 531.6, and 533.9 eV, respectively [31]. The above results indicate that the as-prepared  $\text{MgCo}_2\text{O}_4$  nanochains are pure phase and the graphene is well retained, supporting the results of the XRD and TEM.

### 3.2 Electrochemical properties

The as-prepared  $\text{MgCo}_2\text{O}_4$  arrays/G-NF samples were evaluated as supercapacitor electrodes. Figure 8a shows CV curves for all samples at a scan rate of  $5 \text{ mV s}^{-1}$  between 0 and 0.5 V. For all  $\text{MgCo}_2\text{O}_4$  arrays/G-NF electrodes, distinct redox peaks can be seen, which are originated from the faradaic redox reactions involving M-O/M-O-OH (M refers to Mg or Co) [32]. It is noted that the G-NF electrode exhibited much lower current than that of  $\text{MgCo}_2\text{O}_4$  arrays/G-NF electrodes. Among all electrodes,  $\text{MgCo}_2\text{O}_4$  nanowire arrays/G-NF electrode exhibited the largest area of CV curve, which represents the highest capacitance. Figure 8b shows the CV curves of the  $\text{MgCo}_2\text{O}_4$  nanowire arrays/G-NF electrode from 5 to  $100 \text{ mV s}^{-1}$ . There are a broad oxidative peak located at 0.25 V and a cathodic peak around 0.15 V at a scan rate of  $5 \text{ mV s}^{-1}$ . With the increase of the scan rates, the  $\text{MgCo}_2\text{O}_4$  nanowire arrays/G-NF electrode exhibited similar shape of CV curves, except that the peak currents increase and the position of oxidative/cathodic peak shift towards higher/lower voltage. It indicates that the  $\text{MgCo}_2\text{O}_4$  nanowire arrays/G-NF electrode enables fast redox reactions, which is ascribed to the low resistance of the electrode by growing  $\text{MgCo}_2\text{O}_4$  nanowire arrays on conductive G-NF substrate.

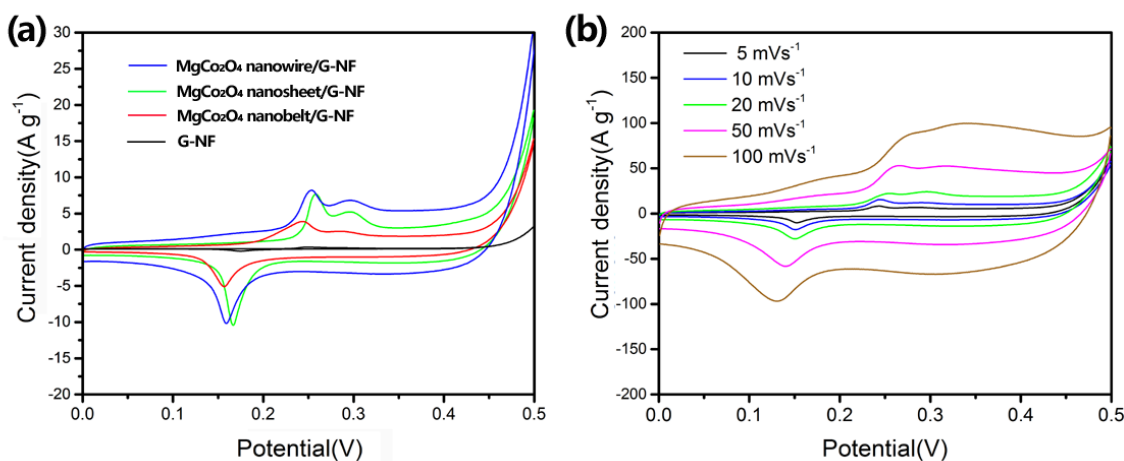


**Figure 8.** (a) CV curves of the  $\text{MgCo}_2\text{O}_4$  nanowire/G-NF, nanosheet/G-NF, nanobelt/G-NF, and G-NF electrodes at a scan rate of  $5 \text{ mV s}^{-1}$  between 0 and 0.5 V; (b) CV curves of the  $\text{MgCo}_2\text{O}_4$  nanowire/G-NF electrode at varied scan rates from 5 to  $100 \text{ mV s}^{-1}$ .

Fig. 9a shows the typical GCD curves of all  $\text{MgCo}_2\text{O}_4$  electrodes at a current density of  $1 \text{ A g}^{-1}$ , as well as G-NF electrode. It is seen that all curves exhibit nonlinear feature with discharge plateaus, which also indicates the existence of faradaic redox reactions. Apparently, the  $\text{MgCo}_2\text{O}_4$  nanowires arrays/G-NF electrode exhibit the longest discharge time than other electrodes do, which indicates that the  $\text{MgCo}_2\text{O}_4$  nanowires arrays/G-NF electrode possesses the highest capacitance. Moreover, the charge–discharge curves of all  $\text{MgCo}_2\text{O}_4$  arrays/G-NF electrodes are almost symmetrical in shape, which indicates that the redox reactions of these electrodes have a superior reversibility. Figure 9b shows the charge-discharge curves for  $\text{MgCo}_2\text{O}_4$  nanowires arrays/G-NF electrode at different current densities. When the current densities increased from 5 to  $50 \text{ A g}^{-1}$ , all curves exhibit a relatively symmetric shape, indicating good pseudocapacitive behaviors. Figure 9c shows the calculated specific capacitances of  $\text{MgCo}_2\text{O}_4$  nanowire arrays/G-NF at varied current densities, as well as those of  $\text{MgCo}_2\text{O}_4$  nanosheet arrays/G-NF and  $\text{MgCo}_2\text{O}_4$  nanobelt arrays/G-NF electrodes. Obviously, the  $\text{MgCo}_2\text{O}_4$  nanowires arrays/G-NF electrode has higher specific capacitance than the other two electrodes at the given current densities.

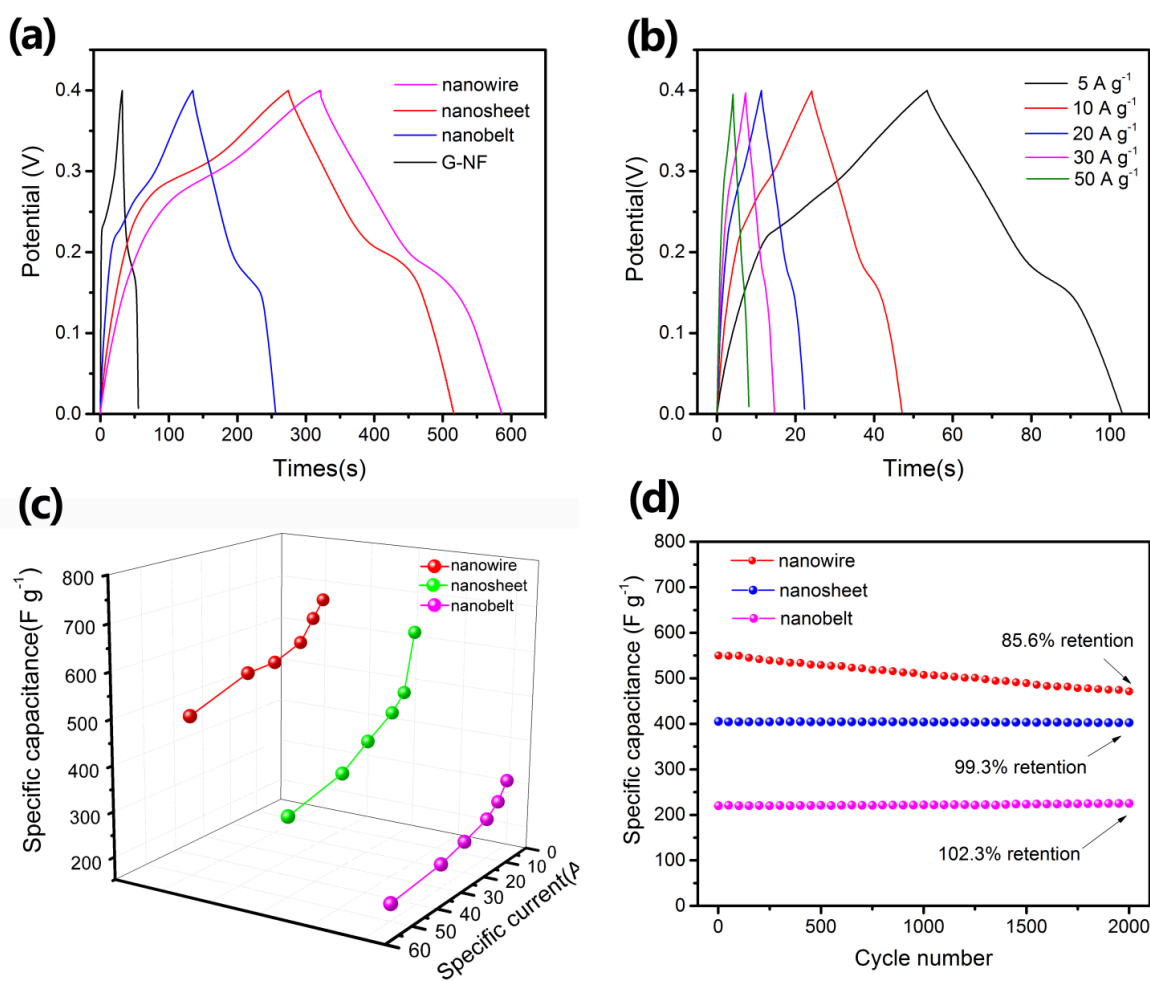


**Figure 9.** (a) Galvanostatic charge–discharge (GCD) curves of all electrodes at the current density of  $1 \text{ A g}^{-1}$ ; (b) the charge-discharge curves for the  $\text{MgCo}_2\text{O}_4$  nanowires arrays/G-NF electrode at varied current densities from 1 to  $50 \text{ A g}^{-1}$ ; (c) calculated specific capacitance under different current densities of three  $\text{MgCo}_2\text{O}_4$  arrays/G-NF electrodes; (d) cycling performance of three  $\text{MgCo}_2\text{O}_4$  arrays/G-NF electrodes.

The MgCo<sub>2</sub>O<sub>4</sub> nanowires arrays/G-NF electrode delivered the specific capacitances of 658, 621, 575, 550, 547, 500 F g<sup>-1</sup> at the current densities of 1, 5, 10, 20, 30, 50 A g<sup>-1</sup>, respectively. The decline in the specific capacitances with increasing current density is because that the electrode active material cannot be effectively utilized at larger current density, which is consistent with previous literatures [33]. It is noted that, with the increasing current density from 1 to 50 A g<sup>-1</sup>, the capacity retention of the MgCo<sub>2</sub>O<sub>4</sub> nanowires arrays/G-NF electrode remains as high as 76 %, showing an excellent rate performance. Figure 9d shows the cycling performances of the three different electrodes at the current density of 20 A g<sup>-1</sup>. In comparison with the other two electrodes, the MgCo<sub>2</sub>O<sub>4</sub> nanowires arrays/G-NF electrode still exhibited the highest specific capacitance of 471 A g<sup>-1</sup> with a capacitance retention ratio of 85.6 % after being cycled 2000 times. As can be seen in Table 1, the rate performance of the MgCo<sub>2</sub>O<sub>4</sub> nanowires arrays/G-NF electrode, especially under high current density, is superior than those of reported MgCo<sub>2</sub>O<sub>4</sub>-based materials, such as MgCo<sub>2</sub>O<sub>4</sub> nanocone/nickel foams (59.4% at 20 A g<sup>-1</sup>), MgCo<sub>2</sub>O<sub>4</sub>/rGO (<73% at 15 A g<sup>-1</sup>), MgCo<sub>2</sub>O<sub>4</sub> hierarchical architectures (56.7% at 20 A g<sup>-1</sup>), MgCo<sub>2</sub>O<sub>4</sub> nanorods (< 15 % at 20 A g<sup>-1</sup>).

**Table 1.** Electrochemical performances of as-prepared MgCo<sub>2</sub>O<sub>4</sub> arrays/G-NF and previously reported MgCo<sub>2</sub>O<sub>4</sub> nanomaterials

Materials	Electrolyte	C <sub>m</sub> (F g <sup>-1</sup> )	Current density	Rate capability	Cycling life (current density)	References
MgCo <sub>2</sub> O <sub>4</sub> nanoparticles	3M LiOH	321	0.5 A g <sup>-1</sup>	56.1% (at 10A g <sup>-1</sup> )	161.5% after 2000 cycles@2 A g <sup>-1</sup>	[20]
MgCo <sub>2</sub> O <sub>4</sub> hierarchical architectures	2M KOH	508	2A g <sup>-1</sup>	56.7% (at 20 Ag <sup>-1</sup> )	95.9% after 2000 cycles @10A g <sup>-1</sup>	[23]
MgCo <sub>2</sub> O <sub>4</sub> cuboidal microcrystals	3M LiOH	690	1A g <sup>-1</sup>	<45% (at 15 Ag <sup>-1</sup> )	116% after 3000 cycles@5A g <sup>-1</sup>	[24]
MgCo <sub>2</sub> O <sub>4</sub> nanorods	2 M KOH	~752	1.3 Ag <sup>-1</sup>	<15 % (at 20 A g <sup>-1</sup> )	Not reported	[19]
MgCo <sub>2</sub> O <sub>4</sub> /rGO	3M LiOH	~570	1A g <sup>-1</sup> (2.5 mA/ cm <sup>2</sup> )	<73% (at 15 A g <sup>-1</sup> )	95% after 5000 cycles@1A g <sup>-1</sup>	[21]
MgCo <sub>2</sub> O <sub>4</sub> nanocone/nickel foams	6M KOH	750	1A g <sup>-1</sup>	59.4% (at 20Ag <sup>-1</sup> )	84% after 1000 cycles @1A g <sup>-1</sup>	[22]
MgCo <sub>2</sub> O <sub>4</sub> nanowires array/G-NF	6M KOH	658	1A g <sup>-1</sup>	76% (at 50 A g <sup>-1</sup> )	85.6% after 2000 cycles@20A g <sup>-1</sup>	This work

Figure 10 shows EIS spectra of three  $\text{MgCo}_2\text{O}_4$  arrays/G-NF electrodes. It is seen that all electrodes exhibit similar spectra, which are featured by a semicircle at high frequency zone and an oblique line at low frequency zone. The EIS spectra are analyzed using the equivalent circuit in the inset of Figure 10. The  $R_s$  can be determined by the intersection value of the semicircle at the real part  $Z'$ . It designates the internal resistance of the solution, which includes the electrolyte resistance, the intrinsic resistance of active electrode materials, and the interface contact resistance between collector and active electrode material. The semicircle diameter reflects the resistance of Faradic charge transfer ( $R_{ct}$ ) and double layer capacitance ( $C_L$ ) [34]. The slope of oblique line represents the Warburg impedance ( $Z_w$ ), which reflects the migration of  $\text{OH}^-$  ions in the electrodes and the transport of proton in the host [35]. It is obvious that the  $\text{MgCo}_2\text{O}_4$  nanowire arrays/G-NF electrode has the lowest value of  $R_s$  and the smallest diameter among three electrodes. Meanwhile, the  $\text{MgCo}_2\text{O}_4$  nanowire arrays/G-NF electrode exhibits a more ideal slope of straight line. Therefore, among three electrodes, the  $\text{MgCo}_2\text{O}_4$  nanowire arrays/G-NF electrode exhibits the largest specific capacitance. The superior high-rate performance of the  $\text{MgCo}_2\text{O}_4$  nanowire arrays/G-NF electrode can be attributed to two factors: (i) The direct growth of the  $\text{MgCo}_2\text{O}_4$  nanowire arrays on conductive graphene-coated nickel foam could ensure every nanowire participates in the ultrafast electrochemical reaction at high current densities. (ii) The 1D mesoporous nanostructure of  $\text{MgCo}_2\text{O}_4$  nanowire arrays can shorten transport path of electron and ion, which leads to the decrease of charge-transfer resistances and ion diffusion resistances, which helps to improve specific capacitance.

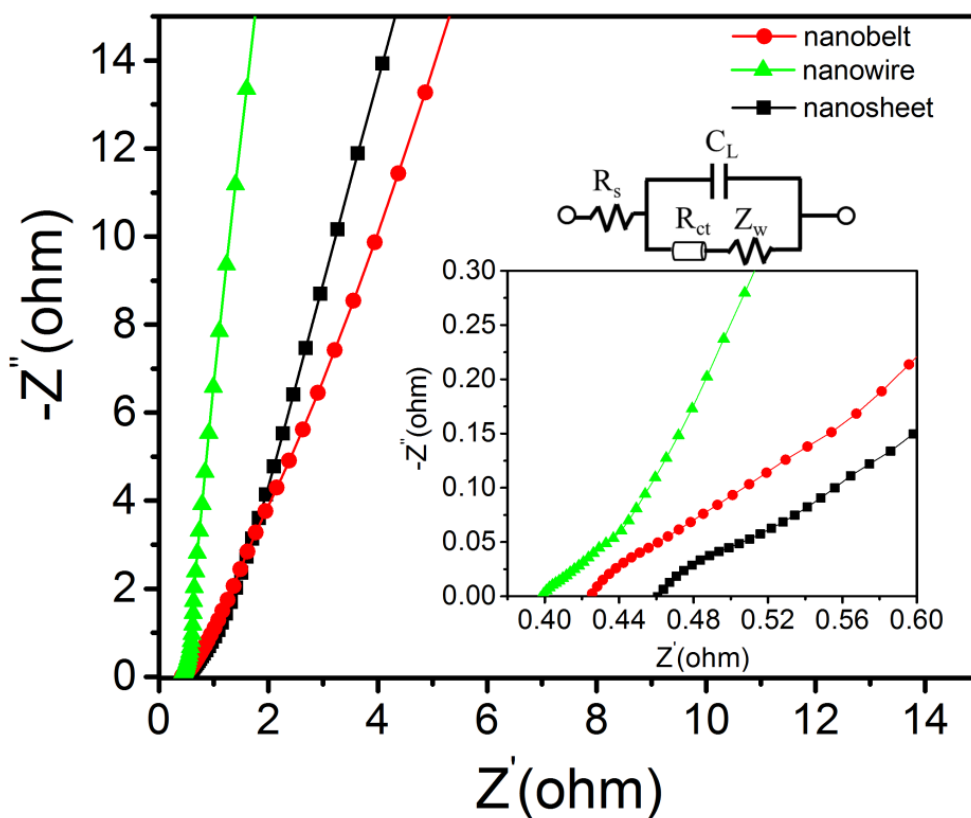


**Figure 10.** EIS and the equivalent circuit of the  $\text{MgCo}_2\text{O}_4$  arrays/G-NF electrodes (the inset shows the enlarged EIS spectra for three electrodes at high frequency zone).

#### 4. CONCLUSIONS

In present work, MgCo<sub>2</sub>O<sub>4</sub> nanosheet, nanobelt, and nanowire arrays on graphene-coated nickel foam were prepared by a facile three-step synthesis. The morphologies of MgCo<sub>2</sub>O<sub>4</sub> arrays can be readily tuned by changing the volume ratio of DEG and deionized water. The as-synthesized MgCo<sub>2</sub>O<sub>4</sub> arrays electrodes are systematically evaluated as electrode materials for supercapacitors. The results show that the MgCo<sub>2</sub>O<sub>4</sub> nanowire arrays/G-NF electrode exhibits superior high-rate electrochemical performance with the optimal specific capacitances of 658, 621, 575, 550, 547, 500 F g<sup>-1</sup> at the current densities of 1, 5, 10, 20, 30, 50 A g<sup>-1</sup>, and good capacitance retention of 85.6 % (2000 cycles at 20 A g<sup>-1</sup>). The superior electrochemical performances are possibly ascribed to the 1D mesoporous nanostructures which shorten the transport path of electron and ion and the direct growth of the MgCo<sub>2</sub>O<sub>4</sub> nanowire arrays on conductive graphene-coated nickel foam, which ensures every nanowire participates in the ultrafast electrochemical reaction at high current densities.

#### ACKNOWLEDGEMENTS

The financial supports of the Natural Science Foundation of Fujian Province (2017J01676, 2017J01677, 2017J01733, 2015J01654, 2015J05091, 2015J01632), the National Natural Science Foundation of China (61376002, 51503036), the Key Research Foundation for Young Scholars of Fujian Education Department of China (JZ160484, JZ160486), and Fujian Education Department of China (JAT160558, JAS150621) are gratefully acknowledged.

#### References

1. L. L. Zhang, X. S. Zhao, *Chem. Soc. Rev.*, 38 (2009) 2520.
2. J. S. Xu, Y. D. Sun, M. J. Lu, L. Wang, J. Zhang, J. H. Qian, E. J. Kim, *J. Alloy. Compd.*, 717 (2017) 108.
3. S. K. Sami, S. Siddiqui, M. T. Feroze, C. H. Chung, *Mater. Res. Exp.*, 4 (2017) 116309.
4. D. L. Li, Y. N. Gong, M. S. Wang, C. X. Pan, *Nano-Micro Lett.*, 9 (2017) 16.
5. S. Vijayakumar, S. Nagamuthu, K. S. Ryu, *Electrochim. Acta*, 238 (2017) 99.
6. L. F. Zhang, W. J. Wang, J. Cheng, Y. H. Shi, Q. Zhang, P. Dou, X. H. Xu, *J. Mater. Sci.*, 53 (2018) 787.
7. J. Kim, J. Lee, J. You, M. S. Park, M. S. Al Hossain, Y. Yamauchi, J. H. Kim, *Mater. Horiz.*, 3 (2016) 517.
8. M. M. Perez-Madrigal, M. G. Edo, C. Aleman, *Green Chem.*, 18 (2016) 5930.
9. E. Ismar, T. Karazehir, M. Ates, A. S. Sarac, *J. Appl. Polym. Sci.*, 135 (2018) 45723.
10. H. Y. Chen, S. Zeng, M. H. Chen, Y. Y. Zhang, Q. W. Li, *Carbon*, 92 (2015) 271.
11. Y. F. Ma, H. C. Chang, M. Zhang, Y. S. Chen, *Adv. Mater.*, 27 (2015) 5296.
12. R. R. Saunkhe, Y. V. Kaneti, Y. Yamauchi, *ACS Nano*, 11 (2017) 5293.
13. M. H. Yu, Z. L. Wang, Y. Han, Y. X. Tong, X. H. Lu, S. H. Yang, *J. Mater. Chem. A*, 4 (2016) 4634.
14. S. K. Chang, Z. Zainal, K. B. Tan, N. A. Yusof, W. M. D. W. Yusoff, S. R. S. Prabaharan, *Ceram. Int.*, 41 (2015) 1.
15. Y. F. Zhang, L. Q. Li, H. Q. Su, W. Huang, X. C. Dong, *J. Mater. Chem. A*, 3 (2015) 43.
16. F. X. Wang, X. W. Wu, X. H. Yuan, Z. C. Liu, Y. Zhang, L. J. Fu, Y. S. Zhu, Q. M. Zhou, Y. P. Wu, W. Huang, *Chem. Soc. Rev.*, 46 (2017) 6816.
17. M. A. Zamudio, S. Bensaid, D. Fino, N. Russo, *Ind. Eng. Chem. Res.*, 50 (2011) 2622.

18. H. Shin, W. J. Lee, *J. Mater. Chem. A*, 4 (2016) 12263.
19. M. Silambarasan, P. S. Ramesh, D. Geetha, V. Venkatachalam, *J. Mater. Sci: Mater. Electron.*, 28 (2017) 6880.
20. S. G. Krishnan, M. V. Reddy, M. Harilal, B. Vidyadharan, I. I. Misnon, M. H. A. Rahim, J. Ismail, R. Jose, *Electrochim. Acta*, 161(2015) 312.
21. S. G. Krishnan, M. Harilal, A. Yar, B. L. Vijayan, J. O. Dennis, M. M. Yusoff, R. Jose, *Electrochim. Acta*, 243 (2017) 119.
22. L. F. Cui, L. H. Huang, M. Ji, Y. G. Wang, H. C. Shi, Y. H. Zuo, S. F. Kang, *J. Power Sources*, 333 (2016) 118.
23. J. S. Xu, L. Wang, J. Zhang, J. H. Qian, J. Liu, Z. Q. Zhang, H. D. Zhang, X. Y. Liu, *J. All. Compd.*, 688 (2016) 933.
24. S. G. Krishnan, M. Harilal, I. I. Misnon, M. V. Reddy, S. Adams, R. Jose, *Ceram. Int.*, 43 (2017) 12270.
25. D. Ji, H. Zhou, J. Zhang, Y. Y. Dan, H. X. Yang, A. H. Yuan, *J. Mater. Chem. A*, 4 (2016) 8283.
26. H. Chen, C. K. Hsieh, Y. Yang, X. Y. Liu, C. H. Lin, C. H. Tsai, Z. Q. Wen, F. Dong, Y. X. Zhang, *ChemElectroChem*, 4 (2017) 2414.
27. Y. Sharma, N. Sharma, G. V. S. Rao, B. V. R. Chowdari, *Solid State Ionics*, 179 (2008) 587.
28. P. Stelmachowski, G. Maniak, J. Kaczmarczyk, F. Zasada, W. Piskorz, A. Kotarba, Z. Sojka, *Appl. Catal. B: Environ.*, 146 (2014) 105.
29. Z. Y. Pu, H. Zhou, Y. F. Zheng, W. Z. Huang, X. N. Li, *Appl. Surf. Sci.*, 410 (2017) 14.
30. Z. Y. Wang, M. Jiang, J. N. Qin, H. Zhou, Z. X. Ding, *Phys. Chem. Chem. Phys.*, 17 (2015) 16040.
31. J. F. Marco, J. R. Gancedo, M. Gracia, J. L. Gautier, E. Rios, F. J. Berry, *J. Solid State Chem.*, 153 (2000) 74.
32. M. Kim, J. Yoo, J. Kim, *J. All. Compd.*, 710 (2017) 528.
33. C. C. Wan, Y. Jiao, J. Li, *J. Power Sources*, 361 (2017) 122.
34. L. Xu, Y. Zhao, J. B. Lian, Y. G. Xu, J. Bao, J. X. Qiu, L. Xu, H. Xu, M. Q. Hua, H. M. Li, *Energy*, 123 (2017) 296.
35. Z. Q. Niu, P. S. Luan, Q. Shao, H. B. Dong, J. Z. Li, J. Chen, D. Zhao, L. Cai, W. Y. Zhou, X. D. Chen, *Energy Environ. Sci.*, 5 (2012) 8726.

© 2018 The Authors. Published by ESG ([www.electrochemsci.org](http://www.electrochemsci.org)). This article is an open access article distributed under the terms and conditions of the Creative Commons Attribution license (<http://creativecommons.org/licenses/by/4.0/>).